Octave-spanning hyperspectral coherent diffractive imaging in the extreme ultraviolet range

Yijian Meng, Chunmei Zhang, Claude Marceau, A. Yu. Naumov, P. B. Corkum and D. M. Villeneuve*

Joint Attosecond Science Laboratory, National Research Council of Canada and University of Ottawa, 100 Sussex Drive, Ottawa, ON K1A 0R6, Canada

*david.villeneuve@nrc.ca

Abstract: Soft x-ray microscopy is a powerful imaging technique that provides sub-micron spatial resolution, as well as chemical specificity using core-level near-edge x-ray absorption fine structure (NEXAFS). Near the carbon K-edge (280-300 eV) biological samples exhibit high contrast, and the detailed spectrum contains information about the local chemical environment of the atoms. Most soft x-ray imaging takes place on dedicated beamlines at synchrotron facilities or at x-ray free electron laser facilities. Tabletop femtosecond laser systems are now able to produce coherent radiation at the carbon K-edge and beyond through the process of high harmonic generation (HHG). The broad bandwidth of HHG is seemingly a limitation to imaging, since x-ray optical elements such as Fresnel zone plates require monochromatic sources. Counter-intuitively, the broad bandwidth of HHG sources can be beneficial as it permits chemically-specific hyperspectral imaging. We apply two separate techniques – Fourier transform spectroscopy, and lensless holographic imaging – to obtain images of an object simultaneously at multiple wavelengths using an octave-spanning high harmonic source with photon energies up to 30 eV. We use an interferometric delay reference to correct for nanometer-scale fluctuations between the two HHG sources.

OCIS codes: (320.7150) Ultrafast spectroscopy; (190.7110) Ultrafast nonlinear optics; (300.6300) Spectroscopy, Fourier transforms.

References and links

1. A. Sakdinawat and D. Attwood, "Nanoscale X-ray imaging," Nat. Photonics **4**, 840–848 (2010).
2. R. Falcone, C. Jacobsen, J. Kirz, S. Marchesini, D. Shapiro, and J. Spence, "New directions in X-ray microscopy," Contemp. Phys. **52**, 293–318 (2011).
3. H. Ade, X. Zhang, S. Cameron, C. Costello, J. Kirz, and S. Williams, "Chemical contrast in X-ray microscopy and spatially resolved XANES spectroscopy of organic specimens," Science **258**, 972–975 (1992).
4. J. A. Brandes, G. D. Cody, D. Rumble, P. Haberstroh, S. Wirick, and Y. Gelinas, "Carbon K-edge XANES spectromicroscopy of natural graphite," Carbon **46**, 1424–1434 (2008).
5. H. N. Chapman, P. Fromme, A. Barty, T. A. White, R. A. Kirian, A. Aquila, M. S. Hunter, J. Schulz, D. P. DePonte, U. Weierstall, R. B. Doak, F. R. N. C. Maia, A. V. Martin, I. Schlichting, L. Lomb, N. Coppola, R. L. Shoeman, S. W. Epp, R. Hartmann, D. Rolles, A. Rudenko, L. Foucar, N. Kimmel, G. Weidenspointner, P. Holl, M. Liang, M. Barthelmess, C. Caleman, S. Boutet, M. J. Bogan, J. Krzywinski, C. Bostedt, S. Bajt, L. Gumprecht, B. Rudek, B. Erk, C. Schmidt, A. Hömke, C. Reich, D. Pietschner, L. Strüder, G. Hauser, H. Gorke, J. Ullrich, S. Herrmann, G. Schaller, F. Schopper, H. Soltau, K.-U. Kühnel, M. Messerschmidt, J. D. Bozek, S. P. Hau-Riege,

#248145 Received 20 Aug 2015; revised 16 Oct 2015; accepted 16 Oct 2015; published 28 Oct 2015

M. Frank, C. Y. Hampton, R. G. Sierra, D. Starodub, G. J. Williams, J. Hajdu, N. Timneanu, M. M. Seibert, J. Andreasson, A. Rocker, O. Jönsson, M. Svenda, S. Stern, K. Nass, R. Andritschke, C.-D. Schröter, F. Krasniqi, M. Bott, K. E. Schmidt, X. Wang, I. Grotjohann, J. M. Holton, T. R. M. Barends, R. Neutze, S. Marchesini, R. Fromme, S. Schorb, D. Rupp, M. Adolph, T. Gorkhover, I. Andersson, H. Hirsemann, G. Potdevin, H. Graafsma, B. Nilsson, and J. C. H. Spence, "Femtosecond X-ray protein nanocrystallography," Nature **470**, 73–77 (2011).

6. M. M. Seibert, T. Ekeberg, F. R. N. C. Maia, M. Svenda, J. Andreasson, O. Jönsson, D. Odić, B. Iwan, A. Rocker, D. Westphal, M. Hantke, D. P. DePonte, A. Barty, J. Schulz, L. Gumprecht, N. Coppola, A. Aquila, M. Liang, T. A. White, A. Martin, C. Caleman, S. Stern, C. Abergel, V. Seltzer, J.-M. Claverie, C. Bostedt, J. D. Bozek, S. Boutet, A. A. Miahnahri, M. Messerschmidt, J. Krzywinski, G. Williams, K. O. Hodgson, M. J. Bogan, C. Y. Hampton, R. G. Sierra, D. Starodub, I. Andersson, S. Bajt, M. Barthelmess, J. C. H. Spence, P. Fromme, U. Weierstall, R. Kirian, M. Hunter, R. B. Doak, S. Marchesini, S. P. Hau-Riege, M. Frank, R. L. Shoeman, L. Lomb, S. W. Epp, R. Hartmann, D. Rolles, A. Rudenko, C. Schmidt, L. Foucar, N. Kimmel, P. Holl, B. Rudek, B. Erk, A. Hömke, C. Reich, D. Pietschner, G. Weidenspointner, L. Strüder, G. Hauser, H. Gorke, J. Ullrich, I. Schlichting, S. Herrmann, G. Schaller, F. Schopper, H. Soltau, K.-U. Kühnel, R. Andritschke, C.-D. Schröter, F. Krasniqi, M. Bott, S. Schorb, D. Rupp, M. Adolph, T. Gorkhover, H. Hirsemann, G. Potdevin, H. Graafsma, B. Nilsson, H. N. Chapman, and J. Hajdu, "Single mimivirus particles intercepted and imaged with an X-ray laser," Nature **470**, 78–81 (2011).
7. S. Boutet, L. Lomb, G. J. Williams, T. R. M. Barends, A. Aquila, R. B. Doak, U. Weierstall, D. P. DePonte, J. Steinbrener, R. L. Shoeman, M. Messerschmidt, A. Barty, T. A. White, S. Kassemeyer, R. A. Kirian, M. M. Seibert, P. A. Montanez, C. Kenney, R. Herbst, P. Hart, J. Pines, G. Haller, S. M. Gruner, H. T. Philipp, M. W. Tate, M. Hromalik, L. J. Koerner, N. v. Bakel, J. Morse, W. Ghonsalves, D. Arnlund, M. J. Bogan, C. Caleman, R. Fromme, C. Y. Hampton, M. S. Hunter, L. C. Johansson, G. Katona, C. Kupitz, M. Liang, A. V. Martin, K. Nass, L. Redecke, F. Stellato, N. Timneanu, D. Wang, N. A. Zatsepin, D. Schafer, J. Defever, R. Neutze, P. Fromme, J. C. H. Spence, H. N. Chapman, and I. Schlichting, "High-Resolution Protein Structure Determination by Serial Femtosecond Crystallography," Science **337**, 362–364 (2012).
8. R. Xu, H. Jiang, C. Song, J. A. Rodriguez, Z. Huang, C.-C. Chen, D. Nam, J. Park, M. Gallagher-Jones, S. Kim, S. Kim, A. Suzuki, Y. Takayama, T. Oroguchi, Y. Takahashi, J. Fan, Y. Zou, T. Hatsui, Y. Inubushi, T. Kameshima, K. Yonekura, K. Tono, T. Togashi, T. Sato, M. Yamamoto, M. Nakasako, M. Yabashi, T. Ishikawa, and J. Miao, "Single-shot three-dimensional structure determination of nanocrystals with femtosecond X-ray free-electron laser pulses," Nat. Commun. **5**, 4061 (2014).
9. R. L. Sandberg, C. Song, P. W. Wachulak, D. A. Raymondson, A. Paul, B. Amirbekian, E. Lee, A. E. Sakdinawat, C. La-O-Vorakiat, M. C. Marconi, C. S. Menoni, M. M. Murnane, J. J. Rocca, H. C. Kapteyn, and J. Miao, "High numerical aperture tabletop soft x-ray diffraction microscopy with 70-nm resolution," P. Natl. Acad. Sci. **105**, 24–27 (2008).
10. G. Sansone, L. Poletto, and M. Nisoli, "High-energy attosecond light sources," Nat. Photonics **5**, 655–663 (2011).
11. E. Takahashi, Y. Nabekawa, and K. Midorikawa, "Generation of 10- μJ coherent extreme-ultraviolet light by use of high-order harmonics," Optics Lett. **27**, 1920–1922 (2002).
12. T. Popmintchev, M.-C. Chen, D. Popmintchev, P. Arpin, S. Brown, S. Ališauskas, G. Andriukaitis, T. Balčiunas, O. D. Mücke, A. Pugzlys, A. Baltuška, B. Shim, S. E. Schrauth, A. Gaeta, C. Hernández-García, L. Plaja, A. Becker, A. Jaron-Becker, M. M. Murnane, and H. C. Kapteyn, "Bright Coherent Ultrahigh Harmonics in the keV X-ray Regime from Mid-Infrared Femtosecond Lasers," Science **336**, 1287–1291 (2012).
13. S. L. Cousin, F. Silva, S. Teichmann, M. Hemmer, B. Buades, and J. Biegert, "High-flux table-top soft x-ray source driven by sub-2-cycle, CEP stable, 1.85-μm 1-kHz pulses for carbon K-edge spectroscopy," Optics Lett. **39**, 5383–5386 (2014).
14. B. Chen, R. A. Dilanian, S. Teichmann, B. Abbey, A. G. Peele, G. J. Williams, P. Hannaford, L. Van Dao, H. M. Quiney, and K. A. Nugent, "Multiple wavelength diffractive imaging," Phys. Rev. A **79**, 023809 (2009).
15. B. Abbey, L. W. Whitehead, H. M. Quiney, D. J. Vine, G. A. Cadenazzi, C. A. Henderson, K. A. Nugent, E. Balaur, C. T. Putkunz, A. G. Peele, G. J. Williams, and I. McNulty, "Lensless imaging using broadband X-ray sources," Nat. Photonics **5**, 420–424 (2011).
16. G. Genoud, O. Guilbaud, E. Mengotti, S.-G. Pettersson, E. Georgiadou, E. Pourtal, C.-G. Wahlström, and A. L'Huillier, "XUV digital in-line holography using high-order harmonics," Appl. Phys. B **90**, 533–538 (2008).
17. M. D. Seaberg, D. E. Adams, E. L. Townsend, D. A. Raymondson, W. F. Schlotter, Y. Liu, C. S. Menoni, L. Rong, C.-C. Chen, J. Miao, H. C. Kapteyn, and M. M. Murnane, "Ultrahigh 22 nm resolution coherent diffractive imaging using a desktop 13 nm high harmonic source," Opt. Express **19**, 22470–22479 (2011).
18. M. Kovačev, S. V. Fomichev, E. Priori, Y. Mairesse, H. Merdji, P. Monchicourt, P. Breger, J. Norin, A. Persson, A. L'Huillier, C.-G. Wahlström, B. Carré, and P. Salières, "Extreme Ultraviolet Fourier-Transform Spectroscopy with High Order Harmonics," Phys. Rev. Lett. **95**, 223903 (2005).
19. S. Witte, V. T. Tenner, D. W. Noom, and K. S. Eikema, "Lensless diffractive imaging with ultra-broadband table-top sources: from infrared to extreme-ultraviolet wavelengths," Light Sci. Appl. **3**, e163 (2014).
20. D. Gauthier, M. Guizar-Sicairos, X. Ge, W. Boutu, B. Carré, J. R. Fienup, and H. Merdji, "Single-shot Femtosecond X-Ray Holography Using Extended References," Phys. Rev. Lett. **105**, 093901 (2010).

#248145 Received 20 Aug 2015; revised 16 Oct 2015; accepted 16 Oct 2015; published 28 Oct 2015

21. R. L. Sandberg, D. A. Raymondson, C. La-o vorakiat, A. Paul, K. S. Raines, J. Miao, M. M. Murnane, H. C. Kapteyn, and W. F. Schlotter, "Tabletop soft-x-ray Fourier transform holography with 50 nm resolution," Opt. Lett. **34**, 1618–1620 (2009).
22. M. Guizar-Sicairos and J. R. Fienup, "Holography with extended reference by autocorrelation linear differential-operation," Opt. Express **15**, 17592–17612 (2007).
23. H. Bluhm, K. Andersson, T. Araki, K. Benzerara, G. E. Brown, J. J. Dynes, S. Ghosal, M. K. Gilles, H. C. Hansen, J. C. Hemminger, A. P. Hitchcock, G. Ketteler, A. L. D. Kilcoyne, E. Kneedler, J. R. Lawrence, G. G. Leppard, J. Majzlam, B. S. Mun, S. C. B. Myneni, A. Nilsson, H. Ogasawara, D. F. Ogletree, K. Pecher, M. Salmeron, D. K. Shuh, B. Tonner, T. Tyliszczak, T. Warwick, and T. H. Yoon, "Soft X-ray microscopy and spectroscopy at the molecular environmental science beamline at the Advanced Light Source," J. Electron Spectrosc. Relat. Phenom. **150**, 86–104 (2006).
24. H. Ohldag, T. Tyliszczak, R. Höhne, D. Spemann, P. Esquinazi, M. Ungureanu, and T. Butz, "Pi-Electron Ferromagnetism in Metal-Free Carbon Probed by Soft X-Ray Dichroism," Phys. Rev. Lett. **98**, 187204 (2007).
25. H. J. Wörner, J. B. Bertrand, D. V. Kartashov, P. B. Corkum, and D. M. Villeneuve, "Following a chemical reaction using high-harmonic interferometry," Nature **466**, 604–607 (2010).
26. Y. Nabekawa, H. Hasegawa, E. J. Takahashi, and K. Midorikawa, "Production of Doubly Charged Helium Ions by Two-Photon Absorption of an Intense Sub-10-fs Soft X-Ray Pulse at 42 eV Photon Energy," Phys. Rev. Lett. **94**, 043001 (2005).
27. D. Descamps, C. Lyngå, J. Norin, A. L'Huillier, C.-G. Wahlström, J.-F. Hergott, H. Merdji, P. Salières, M. Bellini, and T. W. Hänsch, "Extreme ultraviolet interferometry measurements with high-order harmonics," Optics Lett. **25**, 135–137 (2000).
28. J. Miao, P. Charalambous, J. Kirz, and D. Sayre, "Extending the methodology of X-ray crystallography to allow imaging of micrometre-sized non-crystalline specimens," Nature **400**, 342–344 (1999).
29. D. Shapiro, P. Thibault, T. Beetz, V. Elser, M. Howells, C. Jacobsen, J. Kirz, E. Lima, H. Miao, A. M. Neiman, and D. Sayre, "Biological imaging by soft x-ray diffraction microscopy," P. Natl. Acad. Sci. **102**, 15343–15346 (2005).
30. K. S. Raines, S. Salha, R. L. Sandberg, H. Jiang, J. A. Rodríguez, B. P. Fahimian, H. C. Kapteyn, J. Du, and J. Miao, "Three-dimensional structure determination from a single view," Nature **463**, 214–217 (2010).
31. D. Brida, C. Manzoni, and G. Cerullo, "Phase-locked pulses for two-dimensional spectroscopy by a birefringent delay line," Opt. Lett. **37**, 3027–3029 (2012).
32. K. T. Kim, D. M. Villeneuve, and P. B. Corkum, "Manipulating quantum paths for novel attosecond measurement methods," Nat. Photonics **8**, 187–194 (2014).

1. Introduction

Soft x-ray microscopy [1, 2] is an established technique for imaging nanometer-scale objects. The x-ray spectral transmission near the carbon K-edge contains information on the chemical structure [3, 4]. Imaging of sub-micron sized objects that cannot be easily crystallized is a problem that has been addressed with intense x-ray free electron laser (XFEL) facilities. These sources generate enough photons to produce a diffraction image in a single shot [5–8]. However, due to the scale and cost of XFEL facilities, they are not very accessible to researchers. High harmonic sources are tabletop systems that have been employed for coherent diffractive imaging [9]. HHG fluxes have exceeded 10 μJ [10, 11], photon energies have reached beyond 1 keV [12] and NEXAFS resolution has been demonstrated at the carbon K-edge [13]. These sources have excellent spatial and temporal coherence, but their broad bandwidth is seen to be problematic for coherent diffractive imaging, because the imaging resolution is proportional to the bandwidth. Using a broadband HHG source with distinct harmonic peaks, one can oversample the diffraction pattern and retrieve an image as if from a quasi-monochromatic source [14, 15], but this approach requires that the sample is spectrally flat, i.e. monochromatic, and does not contain spectral information. Otherwise, the spectrum must be filtered by narrowband dielectric mirrors [16, 17], resulting in a loss of photon flux, and the loss of all spectral information.

Here we utilize the full bandwidth of an HHG source by applying Fourier transform spectroscopy (FTS) [18, 19] at every pixel in the diffraction image. FTS does not employ slits, so all the photons from the entire spectrum are used to form an image. In our experiment, two synchronized HHG sources are delayed relative to each other with attosecond accuracy and

#248145 Received 20 Aug 2015; revised 16 Oct 2015; accepted 16 Oct 2015; published 28 Oct 2015

focused onto a sample. The resulting far-field diffraction pattern is recorded for each time delay. At each pixel, the time delay trace is Fourier-transformed to provide the spectrum at that pixel – a hyperspectral image. By digitally filtering the image, a series of monochromatic diffraction patterns is obtained. Each diffractive image can be deconvolved using phase retrieval algorithms to give the image of the original sample at that wavelength.

Both parts of our experiment – Fourier transform spectroscopy in the XUV range, and holographic imaging – have been previously demonstrated, but not together. The technique for X-UV hyperspectral imaging was demonstrated by Witte et al. [19] who used Fourier transform spectroscopy with three harmonics from a high harmonic source to form an image of a 300-μm-pitch nickel grid in the Fresnel zone. They developed an algorithm to reconstruct the image by using all 3 harmonic orders, achieving a resolution of 6.7 μm. Fourier transform holographic imaging has been demonstrated with a single XUV frequency [20, 21].

Here, we make two advancements based on this previous work [19]. First, we have performed an XUV hyperspectral imaging experiment in the Fraunhofer regime using Fourier transform holography with an extended holographic reference [22]. Spectral and spatial information are retrieved simultaneously, and image reconstruction does not assume a monochromatic sample.

Second, to the best of our knowledge, this is the first experiment to use an interferometric delay reference in a XUV FTS setup. A delay jitter of a tenth of a wavelength in FTS can deteriorate the quality of retrieved power spectrum [18]. The accuracy of the delay step limits the highest optical frequency that can be spectrally resolved. As shown in our experiment, the use of an interferometric delay reference significantly mitigates problems due to mechanical vibrations and atmospheric turbulence. The referencing setup can be easily implemented to extend the highest resolvable frequency in FTS, which will be essential to future implementations of soft x-ray FTS experiments.

The present experiment is limited in photon energy to about 40 eV due to the use of an 800 nm laser to generate the harmonics. Longer wavelength laser drivers can produce higher photon energies [12]. In the future our technique might be applied to hyperspectral imaging of biological samples near the carbon K-edge [23] or of magnetic materials in the regions of 700 eV (K edge) or 300 eV (L edge) [24]. This will require sub-nanometer accuracy in the delay error between the two sources, which can be addressed by our delay referencing approach.

2. Experiment

We rely on the remarkable temporal accuracy of HHG sources. It has been shown that two sources have relative timing jitter in the zeptosecond range [25]. Since beamsplitters are not readily available in the HHG spectral range, and spatial wavefront division cannot create two closely-separated sources [26], we instead split the driving infrared femtosecond laser pulse and create two separate foci in the same gas source [18, 19, 27]. The two 800-nm 50-fs laser pulses are delayed in a common-path arrangement with a time-delay step size of 27 attoseconds over a total delay of 27 fs. Since splitting the incoming beam spatially results in slightly different focal spots and since timing jitter is introduced by propagating spatially separated replicas in air, we use a pair of Wallaston prisms to delay orthogonal polarization components. The experimental setup is shown in Fig. 1 and explained in more detail in Appendix A.

In Fourier transform spectroscopy, the power spectrum is obtained by recording the autocorrelation trace at uniform delay steps. In our experiment, the autocorrelation trace is collected by changing the path difference between two identical beams using a birefringent interferometer setup. The quality of the retrieved power spectrum depends on the accuracy of the delay steps and the interferometric stability of the optical setup. Fluctuations in the interferometric path length of less than $\lambda/10$ can degrade the spectral resolution [18]. To retrieve wavelengths in the XUV range, the delay accuracy needs to be a few nanometers. We address this technical

#248145 Received 20 Aug 2015; revised 16 Oct 2015; accepted 16 Oct 2015; published 28 Oct 2015

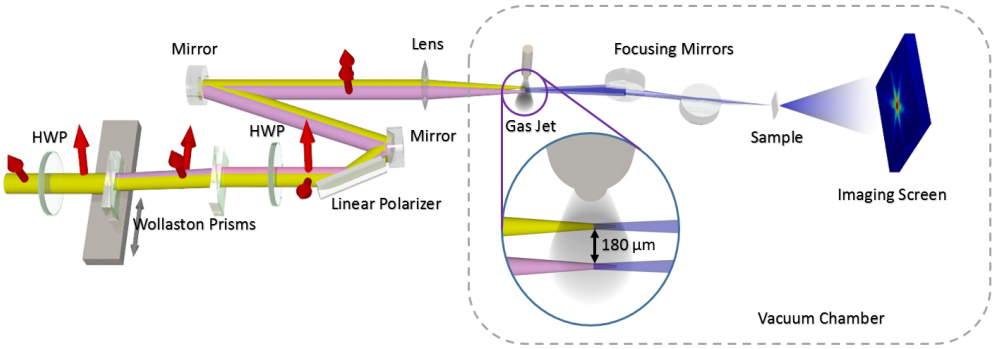

Fig. 1. Experimental setup for Fourier transform coherent diffractive imaging. The 800 nm laser beam is split by a pair of Wollaston prisms into two delayed pulses that focus into the gas jet at slightly different positions. High harmonic generation occurs at each focus, resulting in two soft x-ray beams that are focused onto the object. The resulting diffraction pattern is recorded on a microchannel plate. HWP is half waveplate.

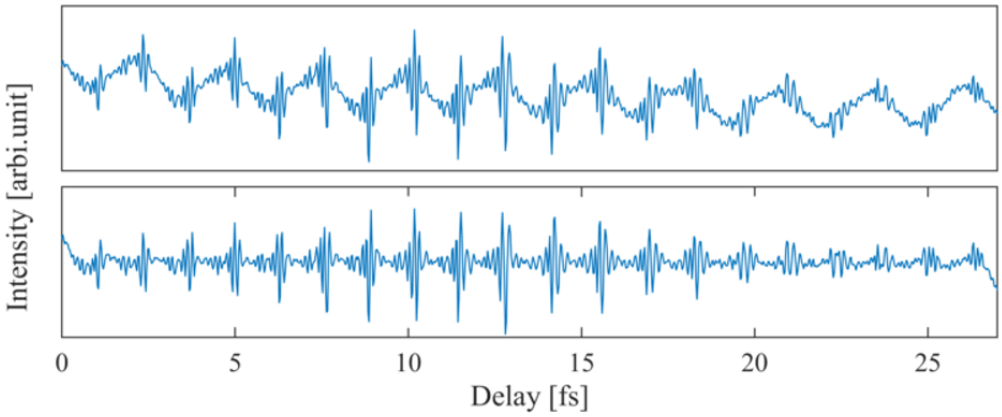

Fig. 2. Fourier transform autocorrelation at a single pixel. At each pixel of the 2D detector, the intensity is recorded as a function of delay between the two high harmonic sources. This trace shows that the HHG signal is composed of a series of attosecond pulses, each separated by half the optical period of the driving laser field. The upper panel is the raw signal recorded at the single pixel, and includes a low-frequency modulation due to a slight overlap of the infrared laser fields on the two focal spots [18]. The lower trace has been high-pass filtered to isolate only the attosecond pulse train contribution.

challenge by using a novel approach based on referencing the delay using optical interference. Part of the two delayed 800 nm laser beams is transmitted through the Brewster plate polarizer and is directed to a second CCD camera, producing interference fringes that move with the relative delay. The position of the fringes is recorded at each delay step, and provides a more accurate measure of the time delay. The measured delay is used to interpolate the autocorrelation trace onto uniform delay steps. This corrects the instability of the optical setup, and corrects for inaccuracy of the translation stage.

The two HHG sources are focused onto a test sample and the far field diffraction pattern is recorded at 1000 relative time delays. Figure 2 shows the intensity vs time delay recorded at

#248145 Received 20 Aug 2015; revised 16 Oct 2015; accepted 16 Oct 2015; published 28 Oct 2015

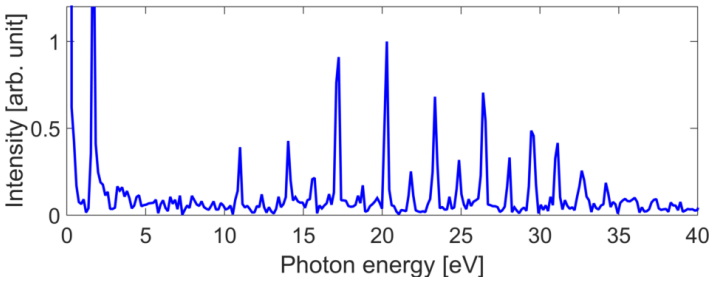

Fig. 3. Spectrum retrieved from a single pixel. A Fourier transform of the time domain signal, such as that shown in Fig. 2, to the frequency domain results in the spectrum shown. The peaks at ω_L and $2\omega_L$ (1.5 and 3 eV) and the weak even harmonics are due to incomplete separation of the two infrared foci, resulting in a modulation of the harmonic yield of each beam as the delay is varied over one optical cycle [18].

a single pixel in the image. This is effectively an autocorrelation of the attosecond pulse train emitted from each HHG source, and illustrates that the signal is a series of attosecond pulses.

The signal at each detector pixel such as that shown in Fig. 2 is Fourier-transformed from the time-domain to the frequency-domain to give the spectrum incident on that pixel. A sample spectrum from a single pixel is shown in Fig. 3. The spectrum at each pixel is digitally filtered to yield a series of hyperspectral images. In Fig. 4 we show the digitally-filtered diffractive images corresponding to harmonics 7, 11 and 17, as well as an image of the test sample. The spatial frequency of the interference fringes is seen to depend on the wavelength corresponding to each harmonic order.

At each optical frequency, the image of the sample can be retrieved from these diffraction patterns. One approach is image reconstruction by iterative phase retrieval [19, 28, 29]. A second approach is Fourier transform holography, where a known reference structure is added to the object to produce a holographic diffraction pattern [22]. This has the advantage that the reconstruction is a single-step deterministic calculation, but requires greater transverse coherence of the optical field. Here we employ the latter approach, Fourier transform holography [22], which has been demonstrated [20, 21] with HHG sources. A micrograph of the test object is shown in Fig. 4. The "unknown" object is the letter "F", and the holographic reference source is a horizontal slit 12 μm wide and 1 μm high.

Thus, we combine Fourier transform holographic imaging and Fourier transform spectroscopy to resolve a test object at a number of soft x-ray wavelengths simultaneously. The reconstruction procedure is described in Appendix A. It results in four images of the same object – one image from each edge of the reference slit, and two conjugate images. The reconstructed images are shown in Fig. 5 at six different harmonic orders. At all harmonic orders, the letter "F" can been seen with good contrast at the top left quadrant along with its conjugate pair at the bottom right quadrant. The second image retrieved at the top right quadrant remains visible at H7 and H9, but starts to distort and blur at the higher harmonic orders. We speculate that the main contributing factor to this effect is the decreasing spatial overlap between the higher order harmonic signal and the reference slit. Since the high harmonic emission from the gas jet is imaged onto the sample, and since the higher order harmonics are emitted from a smaller diameter, the illumination of the reference slit will become less uniform. It might also be caused by imperfections at one end of the reference slit, which ideally should be a step function.

#248145 Received 20 Aug 2015; revised 16 Oct 2015; accepted 16 Oct 2015; published 28 Oct 2015

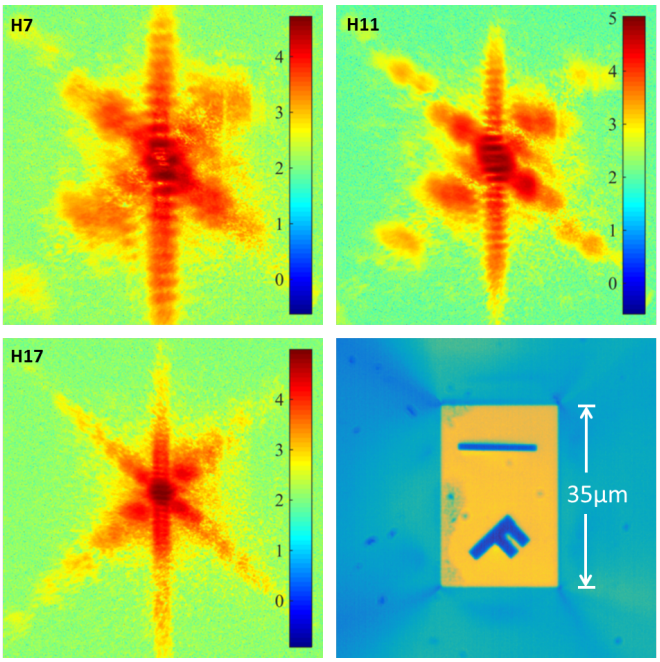

Fig. 4. Frequency-resolved far field diffraction patterns of a test object. The test sample (bottom right) is composed of the letter F and a reference slit. The images shown are digitally filtered to show the diffraction pattern at individual optical frequencies, corresponding to harmonic order 7 (11 eV), 11 (17 eV) and 17 (26 eV). The spectral bandwidth of each image is 0.15 eV, except for H17 where two adjacent frequency elements were averaged. The spatial frequency of the interference pattern is seen to decrease with decreasing wavelength of the harmonic order.

3. Discussion

Since our object is effectively monochromatic, one could also use the redundant information between the six wavelengths to improve the quality [19]. We have not done so here to illustrate the quality of the raw reconstruction. Furthermore, we are interested in imaging objects that are wavelength-dependent, particularly those exhibiting chemical information near x-ray absorption edges. In that case, the images would be different at each wavelength.

The spatial resolution of the retrieved object is determined by three factors: the diffraction limit d_d, the resolution due to the spectral bandwidth d_s, and that due to the size of the reference slit, d_r. The diffraction limit $d_d = \lambda/(2\sin\theta)$ is determined by the range of spatial frequencies collected by the detector, whose numerical aperture is ≈ 0.06. The spectral resolution is given by the fact that the apparent size of the retrieved object is inversely proportional to the wavelength – any spectral bandwidth will blur the image. If D is the largest dimension of the object, then $d_s = D\Delta\lambda/\lambda$. The spectral bandwidth is determined by the 27 fs maximum time delay between the two HHG sources, giving $\Delta E = 0.15$ eV. Then $d_s = D\Delta E/(q\hbar\omega_L) = 0.1D/q$, where q is the harmonic order. Finally, the smaller dimension of the reference slit ($d_r = 1\,\mu$m in our case) limits the spatial resolution of the reconstruction. For our experimental conditions, the reference slit size is responsible for limiting the resolution to 1 μm for all harmonic orders. The magnified image in Fig. 6 confirms that the resolution is about 1 μm.

Since existing HHG sources cannot compare with the brightness of XFELs, a large number

#248145 Received 20 Aug 2015; revised 16 Oct 2015; accepted 16 Oct 2015; published 28 Oct 2015

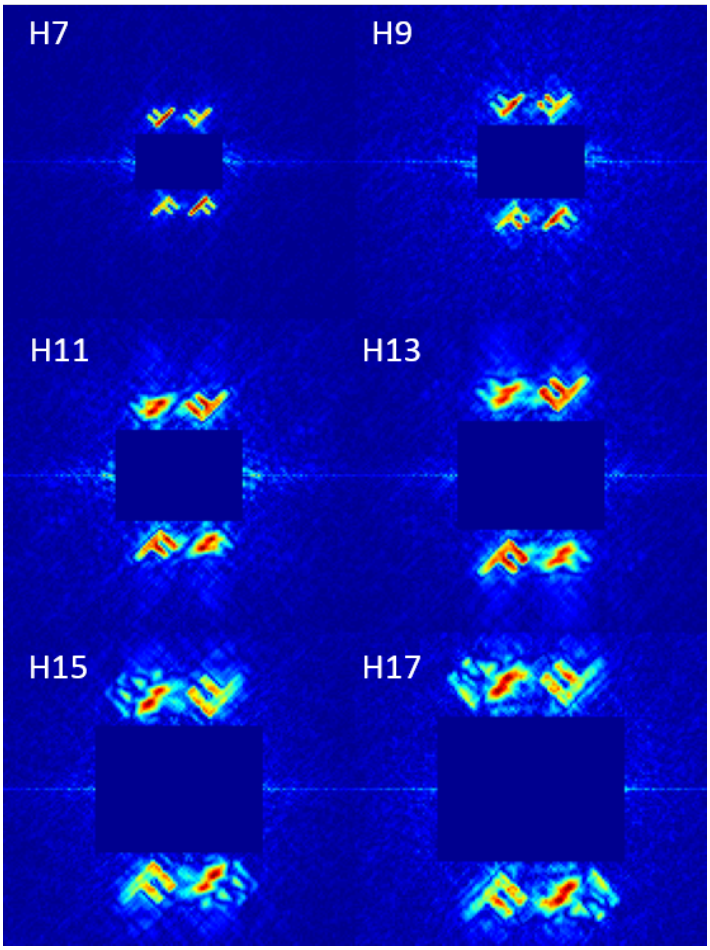

Fig. 5. Reconstructed spatial images of the object. At each optical frequency, a spatial image of the object is reconstructed using an algorithm based on Fourier transform holography with an extended reference. In each image there are four copies of the letter F of the object due to the algorithm. As the wavelength of the radiation becomes shorter (higher harmonic order), the magnification of the image increases. The central part of the reconstruction contains derivatives of the autocorrelation of the object and is masked for clarity.

#248145 Received 20 Aug 2015; revised 16 Oct 2015; accepted 16 Oct 2015; published 28 Oct 2015

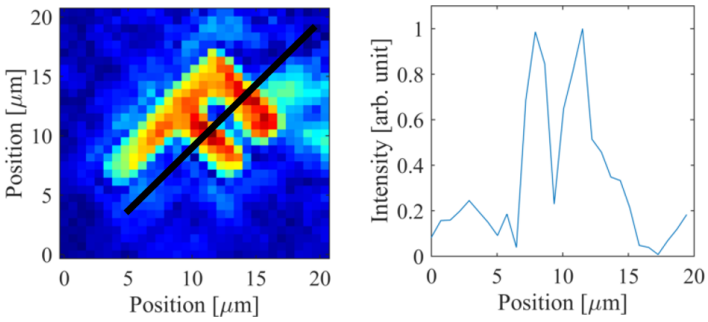

Fig. 6. Magnification of a single reconstructed object. One of the reconstructed objects from Fig. 5, frequency-resolved at harmonic order 13, is magnified here. The spatial resolution is about 1 μm. The resolution is mainly limited by the size of the reference slit, 1 μm.

of laser shots is usually required to produce a diffraction pattern [17]. Therefore the necessity of recording over a number of time delays for FTS comes at no additional cost. When using a spectrally filtered HHG source, the coherence length [21] is $\lambda^2/\Delta\lambda$, limiting the size of the object and the spatial frequency range of the diffraction pattern, as well as reducing the number of photons. With FTS, the spectral resolution is dictated numerically by the total retardation, allowing greater longitudinal coherence lengths. Even narrow spectral features associated with transient absorption can be resolved, given a sufficiently long delay scan.

The HHG photon energy with the present proof-of-principle setup is limited to about 40 eV by the 800 nm laser wavelength and the relatively long 50 fs pulse duration. The photon energy cutoff can be extended to the carbon K-edge at 284 eV and beyond 1 keV by using shorter laser pulses and longer laser wavelengths [12]. Although the spectra that we used here to demonstrate our approach are limited to discrete harmonics, the spectra associated with photon energies in the water window are essentially continuous, and will permit chemical-sensitive imaging near the carbon K-edge [13]. Diffractive imaging at multiple wavelengths might also enable imaging of three-dimensional objects because multiple radii of the Ewald sphere are measured [30].

Appendix A: Methods

We use 5 mJ of an 800 nm driving beam from a 50 fs, 16 mJ, Ti:sapphire laser at 100 Hz repetition rate. We implement an inline-delay setup using birefringent materials similar to Ref. [31] (see Fig. 1). The first half-waveplate rotates the beam polarization by 45°. A pair of Wollaston prisms with 5° wedge angle separates the two polarizations into different propagation angles. By translating the first Wollaston prism perpendicular to the beam direction with a translation stage (Newport MFA-PPD), we can vary the delay between the vertically and horizontally polarized beams. The minimum incremental motion of 100 nm corresponds to $\sim$ 10 asec of actual optical delay per minimum delay step. The second Wollaston prism is used to fine tune the angle between the two beams. The second waveplate rotates the polarization of the two beams by 45°. A Brewster angle linear polarizer is used to produce two vertically polarized beams. We use the light transmitted through the linear polarizer as a delay reference beam (see below), while the reflected light is directed into the vacuum chamber .

A 300 mm focal length lens produces two foci inside a continuous gas jet ($\sim$ 0.3 mm thick) in a vacuum chamber. The gas jet uses argon gas with 1.5 bar of backing pressure. To avoid cross modulation [18,32], the two foci are spatially separated at the gas jet by 180 μm. This produces two identical but separate XUV attosecond pulse trains. The XUV beams propagate 1 m into

#248145 Received 20 Aug 2015; revised 16 Oct 2015; accepted 16 Oct 2015; published 28 Oct 2015

a detector chamber. The XUV is focused with two spherical mirrors (radius of curvature 5 m and 3 m) at grazing angles of 3-5 degrees. The first mirror focuses in the horizontal direction and the second mirror in the vertical direction. The test sample of 35 μm size is placed a few millimeters after the XUV focus to ensure even illumination by both XUV beams. The sample is made from 100 nm thick SiN, coated with a few nm of gold and cut through to form the pattern. The sample is mounted on a 3-dimensional translation stage inside the detector chamber.

The XUV diffraction pattern is recorded 25 cm behind the sample, using a microchannel plate (MCP) of diameter 75 mm and 10 μm pore size, a phosphor screen, and a high dynamic range CCD camera. The CCD camera (model PCO 1600) records a 1.5 cm square of the phosphor screen at 14 bit depth and 20 μm spatial resolution. For each delay, we record the diffraction images by integrating 10 frames each with 2 seconds exposure time. This is equivalent to illumination with $\sim 10^{11}$ XUV photons at each delay. The total delay is 27 fs, which gives a 0.15 eV spectral resolution.

Here we summarize the mathematical method used to obtain the reconstruction from the diffraction pattern at each wavelength. It is based on ref. [22]. Let $f(x,y) = o(x,y) + r(x,y)$ be the optical field exiting the sample. Here $o(x,y)$ is the unknown object and $r(x,y)$ is the known reference slit, parallel to the x-axis. Assuming Fraunhofer diffraction, the far-field amplitude $F(u,v)$ is proportional to the spatial Fourier transform of the near-field amplitude:

$$F(u,v) \propto \int\int f(x,y)\, e^{i2\pi(ux+vy)}\, dxdy \tag{1}$$

Here $u = x'/(\lambda z')$ and $v = y'/(\lambda z')$ are the spatial frequencies, λ is the wavelength of the optical field, x' and y' are the transverse coordinates in the detector plane at distance z' from the object.

By the Wiener-Khintchine theorem, the inverse Fourier transform of the squared modulus of the Fourier transform of a function is the autocorrelation of that function:

$$\mathscr{F}^{-1}\left[|F(u,v)|^2\right] = f \otimes f = o \otimes o + r \otimes r + o \otimes r + r \otimes o \tag{2}$$

If we apply the linear operator $\partial/\partial x$ in the direction x parallel to the reference slit axis, then we obtain two delta functions corresponding to the ends of the slit of length L. Then eq. 2 becomes

$$\frac{\partial}{\partial x}\mathscr{F}^{-1}\left[|F(u,v)|^2\right] = \frac{\partial}{\partial x}\left(o \otimes o + r \otimes r\right) \tag{3}$$

$$+o(x+L/2, y+y_0) - o(x-L/2, y+y_0) \tag{4}$$

$$-o(-x+L/2, -y+y_0) + o(-x-L/2, -y+y_0) \tag{5}$$

The $\partial/\partial x$ term represents autocorrelations of o and r that are localized in the middle of the image. The derivative in the x direction of the Fourier-transformed far-field intensity contains 4 replicas of the unknown object $o(x,y)$, offset vertically by distance y_0 (distance from reference slit to object) and horizontally by $L/2$ (half-width of reference slit).

The reconstruction procedure is as follows: If $I_{far}(u,v)$ is the measured far-field intensity distribution, then $\mathscr{F}^{-1}(iuI_{far})$ contains 4 images of the object. The reconstructed object is shown in Fig. 5 for each harmonic order. At each frequency, the letter F is seen with varying degrees of fidelity. There are four copies of the object due to the holographic reconstruction. The apparent magnification of each image is inversely proportional to the wavelength of the radiation.

Acknowledgments

The authors would like to acknowledge the help of K. T. Kim, T. J. Hammond, D. Geissler, L. Mercadier, A. Staudte, A. Avery, D. Crane and J. Fraser. We gratefully acknowledge funding from NSERC and AFOSR contract FA9550-13-1-0010.

#248145 Received 20 Aug 2015; revised 16 Oct 2015; accepted 16 Oct 2015; published 28 Oct 2015